Available online at www.sciencedirect.com

jmr&t Journal of Materials Research and Technology

www.jmrt.com.br

Original Article

Surface morphologies and corresponding hardness evolution during nanoscratching

Shuohua Zhang[a], *Xiaoguang Guo*[a,*], *Zhuji Jin*[a], *Renke Kang*[a], *Dongming Guo*[a], *William C. Tang*[b]

[a] *Key Laboratory for Precision and Non-Traditional Machining Technology of Ministry of Education, Dalian University of Technology, Dalian, CO 116024, China*

[b] *The Henry Samueli School of Engineering, University of California, Irvine, CA, CO 92697, USA*

ARTICLE INFO

Article history:
Received 14 November 2019
Accepted 17 January 2020
Available online 11 February 2020

Keywords:
Surface morphology
Scratching hardness
Ploughing hardness
Nano-scratch

ABSTRACT

Machining surface topography is a key factor affecting the properties of optical materials. It is generally accepted that the fracture mode tends to dominate practical concerns on machined parts and the elastic recovery area decreases with the increase of normal load. However, material removal rate is low for ductile zone processing of brittle materials. In this case, pile-up and elastic recovery are key factors for surface quality. In this study, an accurate scratching and ploughing hardness model with consideration of both pile-up and elastic recovery was established based on a series of continuous and constant nanoscratch tests. The hardness evolution mechanism under different nanoscratch deformation modes was then investigated. It was found that, in different modes, hardness values exhibited different characteristics due to the change of elastic recovery rate and the intersection of elastic and plastic states. Further, the mapping relationship between hardness dispersion and surface morphology characteristics was also investigated. The results indicated that high degree of hardness dispersion usually corresponded to modes I and II while stable hardness value represented a steady plastic stage. Based on the intrinsic relationship between evolution of hardness and deformation modes, predicting hardness distribution by in-situ testing data and then adjusting deformation mode in real time would be helpful in optimizing surface quality.

1. Introduction

Hard and brittle materials have been widely used in scintillation detectors and solid-state lasers [1]. In particular, they are ideal hosts for high-power solid-state lasers with promising application prospects [2,3]. However, surface cracks and similar damages are easily introduced during processing of such materials, hampering their potential performance. Therefore, it is crucial to investigate the mechanisms of the evolution of the surface topography during materials processing [4–13]. Nanoscratch testing provides a powerful technique for measuring mechanical and tribological properties. Surface appearance, mechanical, physical and chemical characteristics at the micro- and nano-scales can be ascertained [14–19]. For example, Feng et al. [20] investigated crack initiation, propagation and interaction during single and double scratch

* *Corresponding author.*
E-mail: guoxg@dlut.edu.cn (X. Guo).

https://doi.org/10.1016/j.jmrt.2020.01.064

testing of optical glass BK7. Huang et al. [21] discovered the mechanical behavior, including scratch hardness, scratch resistance, and coefficient of friction from nanoscratch tests, can be improved with grain refinement. Moreover, the surface roughness of the scratch grooves and the distinct morphologies of the nanoscratch debris from each sample revealed that alumina ceramic samples with ultrafine grain size exhibited an increase in plastic deformation capacity at the nano- and micro-scales. Wu et al. [22] investigated deformation behaviors of monocrystalline GaAs induced by nanoscratch, and observed lattice bending for the first time at atomic scale in semiconductor materials. Wasmer et al. [23] performed mechanical deformation by nanoindentation and scratching of gallium arsenide and showed that the low indentation velocity allowed twins to be nucleated and propagated from surface inhomogeneities. However, the complexity of the material's elastic-plastic variation around the indenter has been a limiting factor preventing further interpretation of the material's surface formation mechanisms [24–27].

The pile-up and elastic recovery problems have been investigated extensively. Saha et al. [28] provided a quantitative estimate of the pile-up height though they did not account for the effects of pile-up. Park et al. [29] found that stress distribution was a factor that could promote pile- up on copper surface. They also reported that a graphene layer coated on the surface would enhance the elastic modulus by 5% during the pile-up process. Kucharski et al. [30] established a true hardness model by accounting for a specific pile-up pattern. They showed that hardness–tip radius relationship exhibited a linear form for nominal hardness and bilinear form for true hardness. Zhang et al. [31] established the elastic deformation model considering both elastic extrusion and elastic recovery deformation. The origin of the microcracks was then discussed. In addition, the observed responses of surface quality were shown to depend greatly on the extent of elastic deformation prevalent during the nanoscratch and associated material removal processes. Wang et al. [32] explained the different pile-up patterns through the strong crystallographic anisotropy of the out-of-plane displacements around the indents. However, as of the time of this paper, there seems to be no reports that establish an intrinsic link between the elastoplastic change and the evolution of surface topography during the scratching process.

In this study, the removal characteristics of Lu_2O_3 laser crystals under different scratching speeds and loads were obtained by a series of nanoscratch tests. An accurate hardness model during scratch process was then established based on the experimental data and the contact geometric relationship between the indenter and the sample. Finally, the intrinsic relationship between the change of surface morphology and the evolution of both scratching and ploughing hardness during scratching were investigated.

2. Experiments

First, the Lu_2O_3 laser crystal was cut into the same size samples of 10 mm × 5 mm × 2 mm by Wire Electric Discharge Machining (WEDM). The samples were then grinded and polished by Chemical Mechanical Polishing (CMP) until all the roughness values of the polished surfaces are less than 6 nm as measured by 3-D Surface Profiler (Newview 5022, ZYGO), as shown in Fig. 1.

Table 1 – Experimental parameters.

Tests	Normal load (L) (mN)	Scratching speed (V) (μm·s–1)
1	15	0 – 20
2	0 – 100	1
3	0 – 100	0 – 100
4	15	1, 5, 10, 20, 100
5	1, 5, 15, 50, 100	10

All the nanoscratch tests were performed on Nano Indenter G200 (MTS Systems Corp.) using a diamond Berkovich indenter with edge-forward scratching direction, as shown in Fig. 2. Continuous loading and continuous speeding mode scratch tests were performed to obtain the material removal characteristics under different scratching speeds and loads. Then, to investigate the details of the evolution law of ploughing and scratching hardness during nanoscratching, a series of constant loading and speeding tests were carried out. Specific experimental parameters were listed in Table 1.

3. Results and discussion

3.1. *Effect of normal load and scratching speed on surface morphologies*

Fig. 3 shows the SEM micrographs of typical morphologies of three nanoscratched grooves under different scratch conditions. All three scratches progressed from right to left. In particular, Fig. 3(a) reveals that there were no observable changes in the width of the groove nor any cracks with the increase of scratching speed when the normal load was kept constant. However, it also shows that the chips gradually moved away from the groove. The angle between the shaving and scratch direction also increased with increasing scratching speed.

The SEM image in Fig. 3(b) shows the increase of scratch width with increasing load when the scratching speed is constant. The groove surface changed from smooth to an obvious wave pattern, and finally surface cracks appeared. It was observed that the plastic flow lines along the edge of the groove became increasingly dense and long as the normal load increased. Furthermore, as the normal load continued to increase, edge cracks started to appear on the groove edge and the chips moved farther away from the groove.

It is interesting to note that the scratch direction became unstable when the normal load and scratching speed were changed simultaneously, as shown in Fig. 3(c). The higher the speed, the more severe the path direction deviated. Also, there were more surface cracks in the area where the scratch direction changed, as highlighted in the enlarged image. It is undeniable that the scratch direction at high speed was more sensitive to the change of load, although it might be related to the uniformity of the material. Moreover, the groove widened gradually, and the chip distribution became more dispersed as the load and scratching speed increased. However, compared

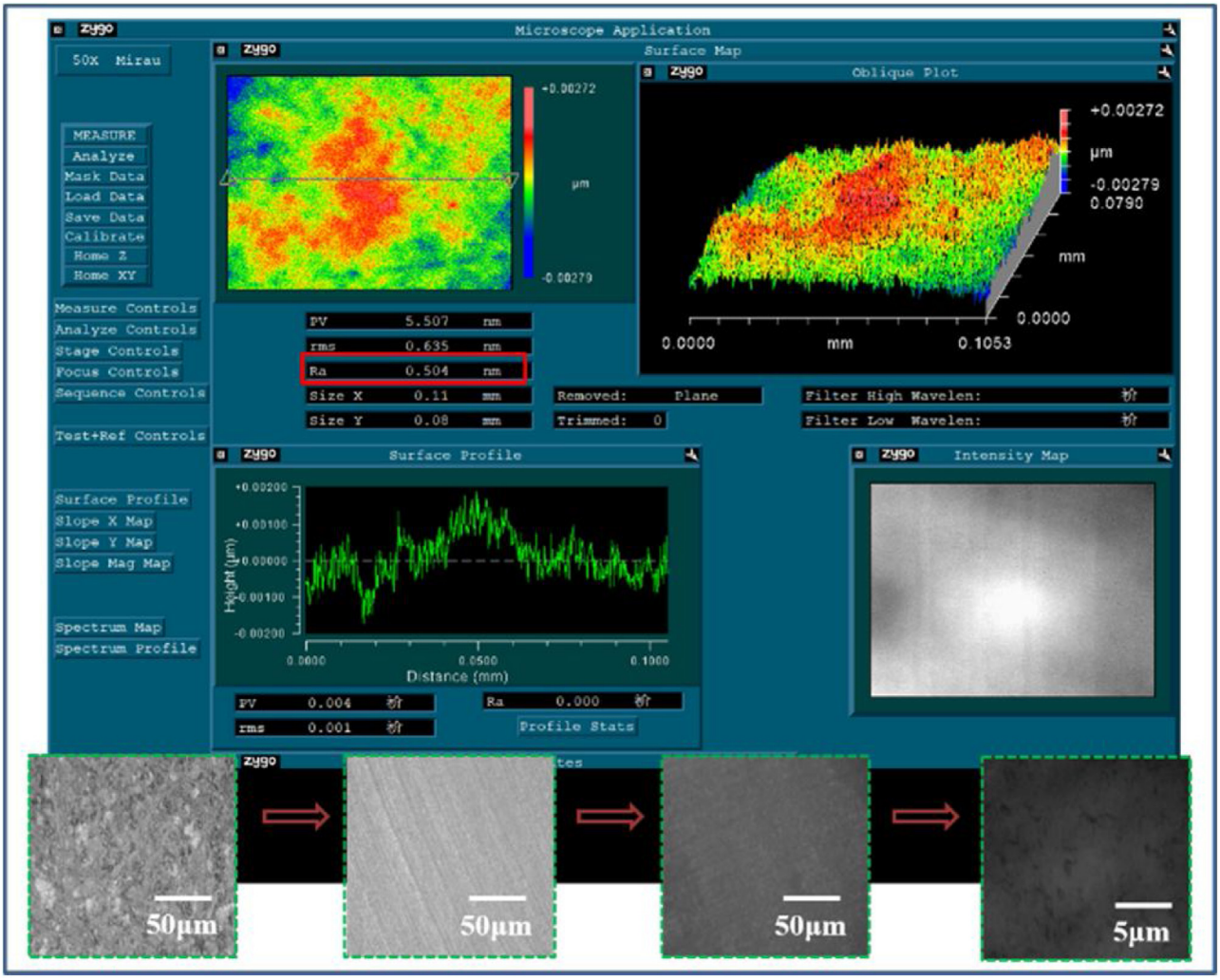

Fig. 1 – Sample preparation.

with Fig. 3(b), the groove surface cracks and edge cracks were significantly reduced.

The experiments shown in Fig. 3 as a whole demonstrated that scratching speed and load greatly affected the surface quality of the material beyond simply determining the material removal rate. It is a common observation that surface quality and removal rate are often conflicting goals in machining. Therefore, it is of great interest to understand the intrinsic mechanism of the influence of scratching speed and load on the mechanical and tribological properties during material removal.

3.2. *Effects of normal load and scratching speed on hardness during nanoscratching*

The pile-up in front of the indenter and the elastic recovery in the rear of the indenter directly affect the contact area between the indenter and the material, as illustrated in Fig. 4(a). In addition, they also greatly affect the precise characterization of the ploughing and scratching hardness. In this study, a more accurate hardness model during scratch process was constructed based on our previous work [31].

As illustrated in Fig. 4(b), the indenter is not strictly an ideal triangular pyramidal in shape, and the top of the indenter is circular. The diagram of the contact region between the indenter and the sample is illustrated in Fig. 4(c). The definitions of the symbols used in Fig. 4(c) are listed in Table 2.

In Fig. 4(c), Δh can be expressed with Eq. (1). The projection of the contact area (S) on the plane where the scratch direction is located and the plane perpendicular to the scratch direction (S_p) can be derived with Eqs. (2) and (3), respectively. The detail derivation steps are included in Appendix A.

$$\Delta h = \frac{R}{\cos\left(\frac{1}{2}(\alpha+\beta)\right)}\cos\left(\frac{1}{2}(\beta-\alpha)\right) - R \tag{1}$$

where R is the radius of the circle at the top of the Berkovich indenter and was 100 nm in this setup. α is the angle between the horizontal plane and the leading edge of the indenter and was found to be 12.75°. β is the angle between the plane and the trailing face at 25.75°.

$$S = \sqrt{3}(h+\Delta h)\tan\left(\frac{\pi}{2}-\alpha\right).$$

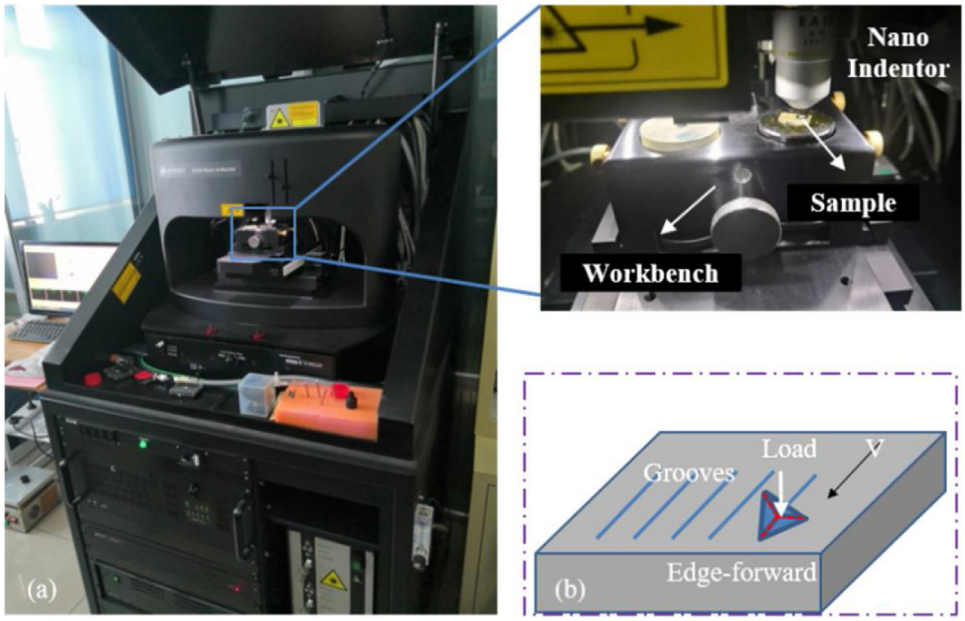

Fig. 2 – (a) Photograph of Nano Indenter G200 used for scratching tests. (b) Diagram of the nanoscratch process.

Table 2 – Definitions of symbols.

Symbol	Definition	Symbol	Definition
h	Penetration depth	Δh	The difference between triangular pyramid and spherical shape in normal direction
h_f	Residual depth	l_{CO}	Distance from the center of the top sphere to the top of the ideal pyramid
h_e	Extrusion deformation height	l_{CB}	Distance between the center of the top sphere and the scratch plane at the top of the triangular pyramid
γ	Included angles between l_{CB} and l_{CO}	S_{c1}	Projected areas in normal direction due to penetration
ζ	Included angles between l_{CA} and l_{CO}	S_{c2}	Projected areas in normal direction due to elastic recovery
S_{p1}	Projected areas in the direction of scratching due to penetration	S_{c3}	Projected areas in normal direction due to pile-up
S_{p2}	Projected areas in the direction of scratching due to pile-up		

$$\left\{\left(h+\Delta h-h_f\right)\left[\tan\left(\frac{\pi}{2}-\beta\right)+\frac{1}{2}\tan\left(\frac{\pi}{2}-\alpha\right)\right]+\frac{1}{2}\left(h+\Delta h\right)\tan\left(\frac{\pi}{2}-\alpha\right)\right\}$$

$$-\left(h+\Delta h-h_f\right)^2\tan^2\left(\frac{\pi}{2}-\beta\right) \quad (2)$$

$$S_p=\left(h+\Delta h+h_f\right)\left(h+\Delta h\right)\tan\left(\frac{\pi}{2}-\beta\right) \quad (3)$$

To verify the accuracy of the contact geometric model above, the residual depth, h_f, was calculated as shown in Eq. (4) with the detail derivation steps listed in Appendix A. The residual depths obtained through the in-situ measurement system of Nano Indenter G200 were compared with the theoretical values derived from the contact geometric relationship (Fig. 5). It can be seen clearly that the theoretical values, except for a slight overestimation overall, were in good agreement with the experimental results, validating the geometric model. Worthy of note is that the experimental values of the residual depth increased sharply as the normal load was increased from zero while showing significant randomness in the initial stage. This phenomenon is discussed in Section 3.

$$h_f=-2.8H_0+\sqrt{-\frac{\left(\frac{h}{144}\right)^{2.5}}{4.3L_m}+\frac{79{H_0}^2}{4.3}} \quad (4)$$

$$\text{Where, } L_m=\frac{2}{3}\frac{H_0}{2.8}\left(\frac{5}{3}+\ln\left(\frac{4(1-2\nu)\frac{H_0}{2.8}+E\tan\psi}{6(1-\nu)\frac{H_0}{2.8}}\right)\right)\cdot\left(m+k\ln\left(\frac{V}{w\bar{\varepsilon}}\right)\right)$$

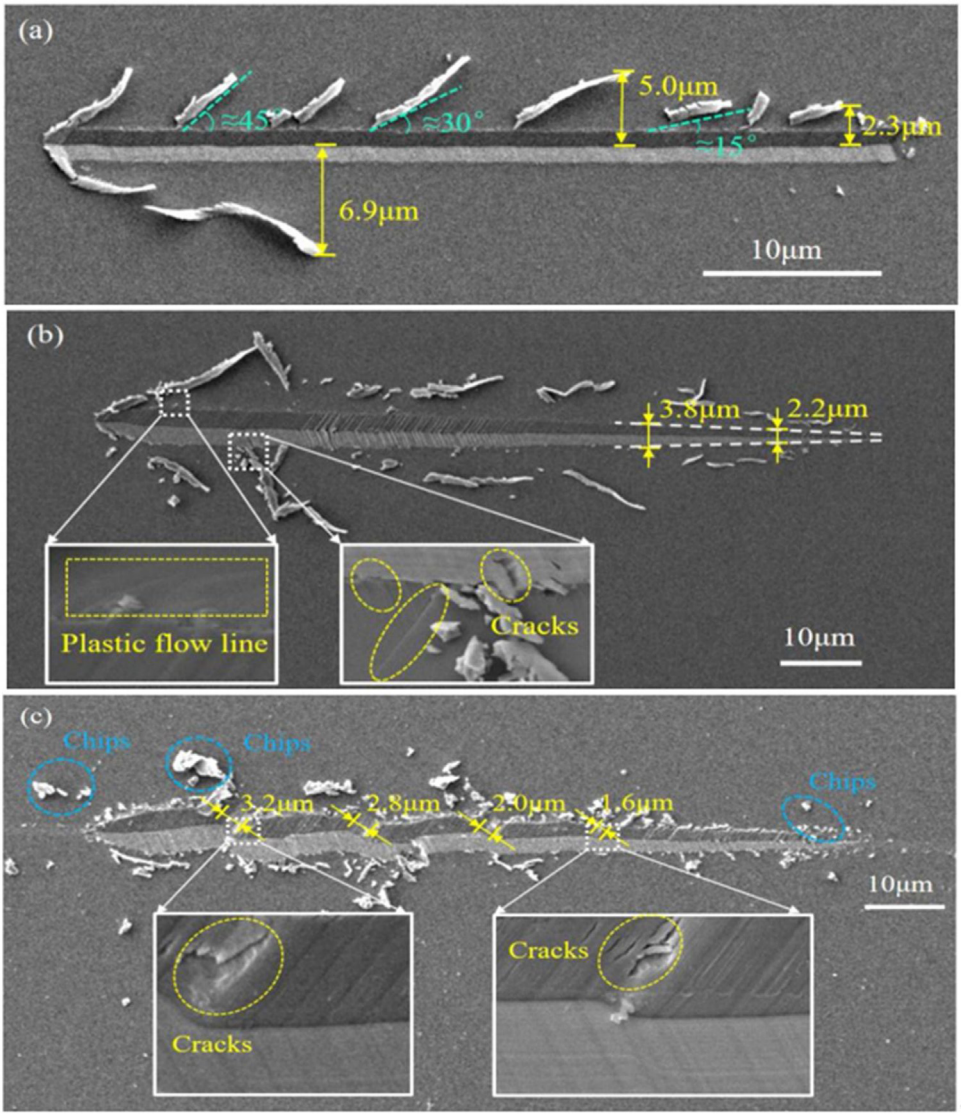

Fig. 3 – Surface characteristics of material removal under continuous parameters. All scratches were from right to left. (a) Scratching speed ranged from 0 to 20 μm·s^{-1} while normal load was 15 mN. (b) Normal load ranged from 0 to 100 mN while scratching speed was 1 μm·s^{-1}. (c) Normal load ranged from 0 to 100 mN while scratching speed ranged from 0 to 100 μm·s^{-1}.

H_0 is the micro hardness can be measured by nano indentation depends on specific experimental parameters of every nano-scratch test, E is the elastic modulus and is about 210 GPa also measured by nano indentation, ν is Poisson ratio, which is 0.3, ψ is 19.7 for Berkovich indenter, V is the scratching speed, w is the width of the scratches, $\dot{\varepsilon}$ is the reference strain rate, m ad k are fitting parameters [2].

The scratching hardness (H) and the ploughing hardness (H_p) considering both pile-up and elastic recovery during scratching process using Berkovich indenter can be expressed as follows, respectively [34–36].

$$H = \frac{L}{S} \tag{5}$$

$$H_P = \frac{L_P}{S_P} \tag{6}$$

where L and L_p are normal load and tangential load, respectively.

The effect of both scratching speed and load on hardness were explored using the relationship above by a series of constant loading and speeding modes. It can be seen in Fig. 6(a) that as the speed increased, the scratching hardness showed a downward trend and then became stable. On the other hand, the ploughing hardness first decreased with the increase of the scratching speed, but increased when the scratching speed increased beyond the critical speed of about 10 μm·s^{-1}. The horizontal projection area increased at first and then did not change significantly with the increase of scratching speed, as shown in Fig. 6(b).

In addition, Fig. 6(b) shows that with the increase of scratching speed, projection of the contact area on the plane perpendicular to the scratch direction first increased rapidly, and then reached a steady state, while the tangential load

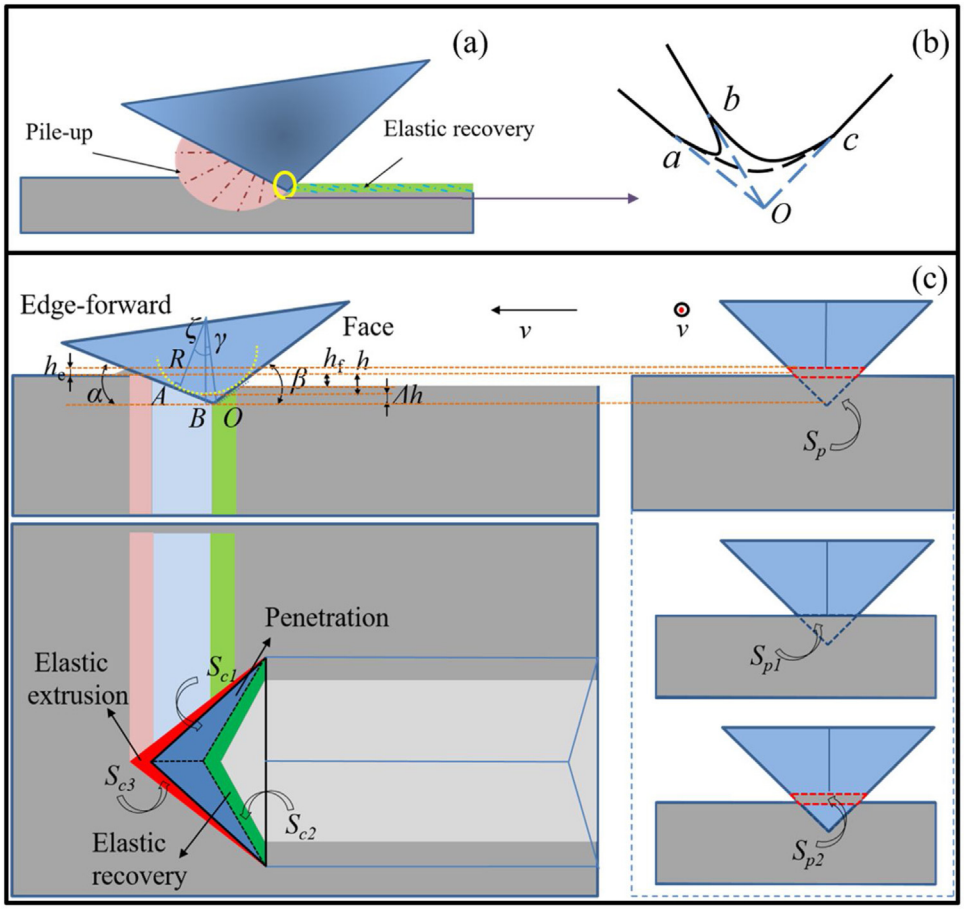

Fig. 4 – (a) Illustration of the pile-up and the elastic recovery around the indenter. (b) The cross-sectional shape of the indenter tip. (c) Illustrations of the contact region between indenter and sample (after [2], Fig. 9 and [33], Fig. 4).

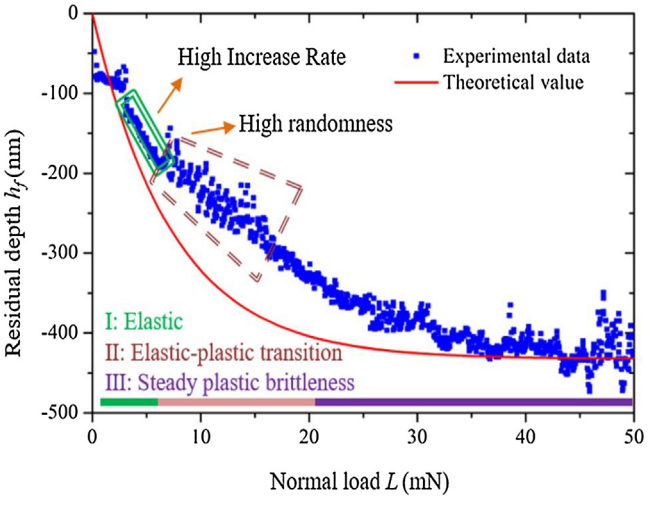

Fig. 5 – Relationship between residual depth and normal force.

changed from slow increase to rapid increase. The calculated results are consistent with the relationship among hardness, projected area, and load.

With the increase of the normal load, both the scratching hardness and ploughing hardness showed initial decrease followed by an asymptotic trend. The difference is that the rate of decline in scratching hardness decreased with increasing load, while the rate of decline in ploughing hardness did not decrease monotonically with increasing load, as shown in Fig. 7(a). This phenomenon can be explained from Fig. 7(b). With the increase of normal load, the projection of the contact area on the plane where the scratch direction increased, and the increase rate of projection area was always higher than that of normal load. Although both the vertical projected area and the tangential load increase with increasing normal load, there was no single size relationship.

3.3. *Relationship between surface morphologies and corresponding hardness evolution*

Tribology property was a crucial factor influencing the surface morphologies. The coefficient of friction (COF) in the ploughing regime can be expressed as follows [2,37,38] with the detailed derivation steps listed in Appendix B. From the expression of COF, it can be seen that both

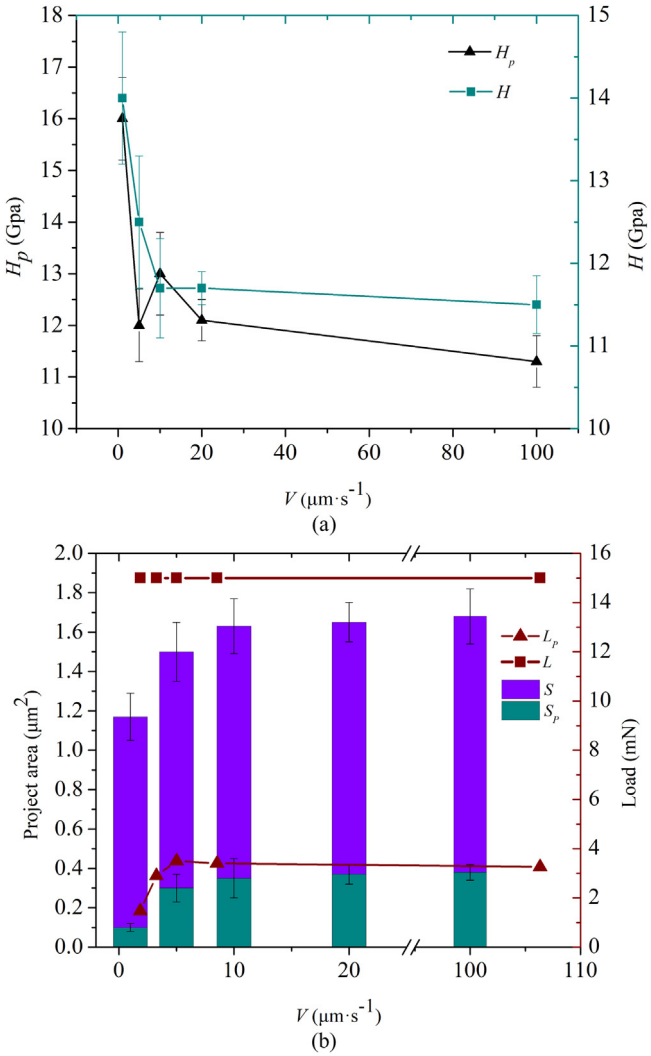

Fig. 6 – (a) Effects of scratching speed on the scratching hardness and ploughing hardness and (b) scratching speed vs. project areas in normal direction, projected areas in the direction of scratching, normal load and tangential load, respectively.

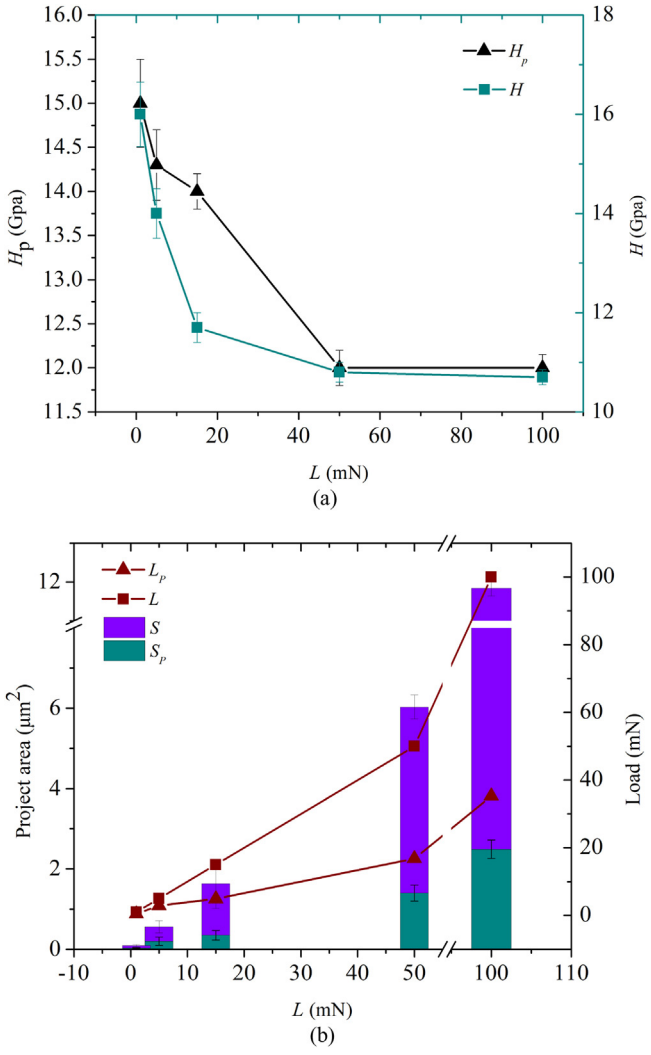

Fig. 7 – (a) Effects of normal load on mechanical parameters and (b) normal load vs. project areas in normal direction, projected areas in the direction of scratching and tangential load, respectively.

scratching speed and normal load played important roles in COF.

$$COF = \frac{\tau S_p}{\lambda_0 \left(m + k \ln\left(\frac{V}{w\dot{\varepsilon}}\right)\right) S} \tag{7}$$

where τ and λ_0 are the stresses in horizontal and vertical orientation, respectively.

COF values under varying load are shown in Fig. 8. It is observed that there are 3 modes of COF. The experimental data indicated that the modes I, II and III corresponded to elastic, elastic-plastic transition and steady plastic brittleness stage, respectively. In mode I, COF decreased sharply with the increase of normal load. Then once the normal load reached the critical load of about 5 mN, COF showed an upward trend. This probably led to the plastic deformation around the indenter in addition to breaking the interfacial shear strength so that the indenter moved horizontally in mode II. Moreover, COF values showed strong fluctuations in these two modes. In mode III, COF reached a relatively steady state.

Further, both ploughing and scratching hardness showed substantial dispersion in modes I and II. This result could be attributed to the change of contact area between the indenter and the sample. In mode I, rapid increase in both pile-up in front of the indenter and elastic recovery in the rear of the indenter led to a sharp increase in contact area, so the hardness dropped significantly. Then in mode II, the intersection of elastic state and plastic state increased the randomness of elastic recovery depth, resulting in the fluctuation of contact area, and ultimately led to the increase of hardness dispersion. This was in agreement with the experimental results as shown in Fig. 5, where residual depth increased sharply in mode I and exhibited high randomness in mode II.

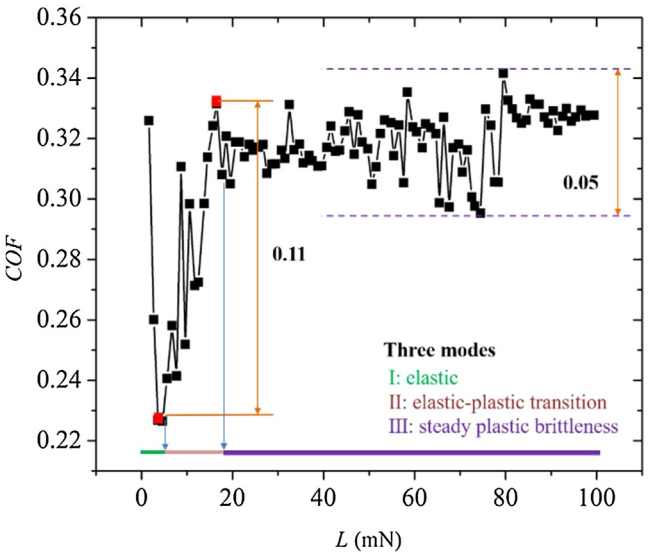

Fig. 8 – COF vs. normal load.

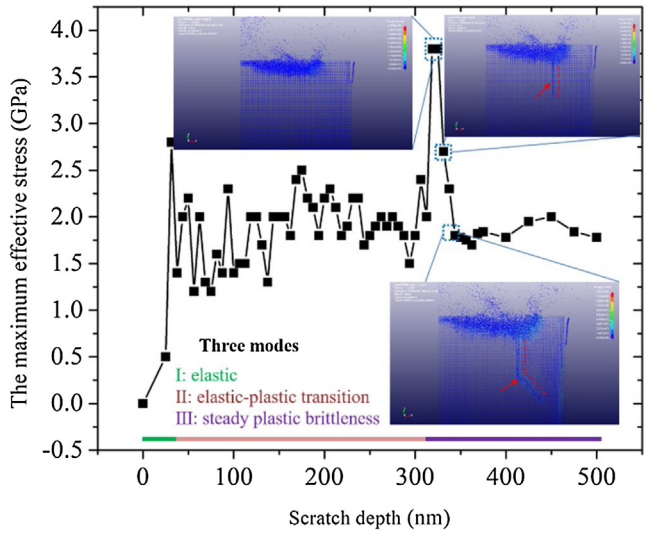

Fig. 9 – The maximum effective stress vs. scratch depth.

Table 3 – Partial material parameters.

Symbol	Definition	Value
H	Micro hardness (GPa)	10.95
E	Elastic modulus (GPa)	210
ρ	Density (g/cm3)	9.42
ν	Poisson ratio	0.3
M	Fractured strength parameter (pressure exponent)	0.35
N	Fractured strength parameter (pressure exponent)	0.77
nT	Total number of particles	400000

Fig. 9 shows the maximum effective stress under continuous depth based on the SPH (smoothed particle hydrodynamics) simulation model of hard and brittle material. Some material parameters are shown in Table 3. In modes I and II, the maximum effective stress fluctuated greatly with the increase of the scratch depth, while the maximum effective stress fluctuation in mode III reached a relatively steady state. The maximum stress reached the peak value before the middle crack appears. With the appearance of the middle and the transverse cracks, the maximum stress droped sharply, which was attributed to the release of energy by crack growth. It can be seen that the fluctuation laws of COF and the maximum effective stress in different modes have good consistency.

Based on the hardness model above and a series of continuous and constant tests, the distributions of both scratching and ploughing hardness values during nanoscratching were calculated. The relationships among the two hardness distributions (H_p and H), scratching speed (V) and normal load (L) were represented with 3D plots as shown in Fig. 10. The corresponding morphologies on the resulting surfaces at several points on the plots were examined with SEM, also shown in Fig. 10. It can be observed that high degrees of hardness dispersion were correlated with smooth surfaces on the scratched grooves, slight plastic flow lines at groove edges and uniform and complete debris, which were in good agreement with modes I and II. On the other hand, low degrees of hardness dispersion were correlated with the relatively poor scratched groove surfaces, where the flow lines were dense and random cracks appeared on the groove edges. In these scenarios, chips were broken and aggregated. All of these features were consistent with mode III. It should be noted that among a large number of tests data collected, there were occasionally some large fluctuations in scratch hardness in a high brittle mode, but this had not adversely affected the overall conclusion of this work, especially for ductile zone processing.

4. Conclusions

In this work, a more accurate scratching and ploughing hardness model was constructed by considering both pile-up and elastic recovery in a series of continuous and constant nanoscratch tests. the hardness evolution mechanism under different nanoscratch deformation modes was investigated. The relationships among the two hardness distributions, scratch speed, and normal load were established with corresponding surface morphologies. The main conclusions were summarized below:

1. In different modes, pile-up and elastic recovery exhibit different characteristics and affect the distribution of scratching and ploughing hardness values especially in modes I and II.

2. The hardness values show high dispersion due to the change of elastic recovery rate and the intersection of elastic and plastic states in modes I and II. However, the hardness values show stability after reaching the steady plastic stage.

3. The relationships among hardness distributions, scratching speed, and normal load can be represented in 3D plots with the corresponding surface morphologies at several points obtained using SEM. In general, high degree of hardness dispersion is correlated with smooth surfaces on

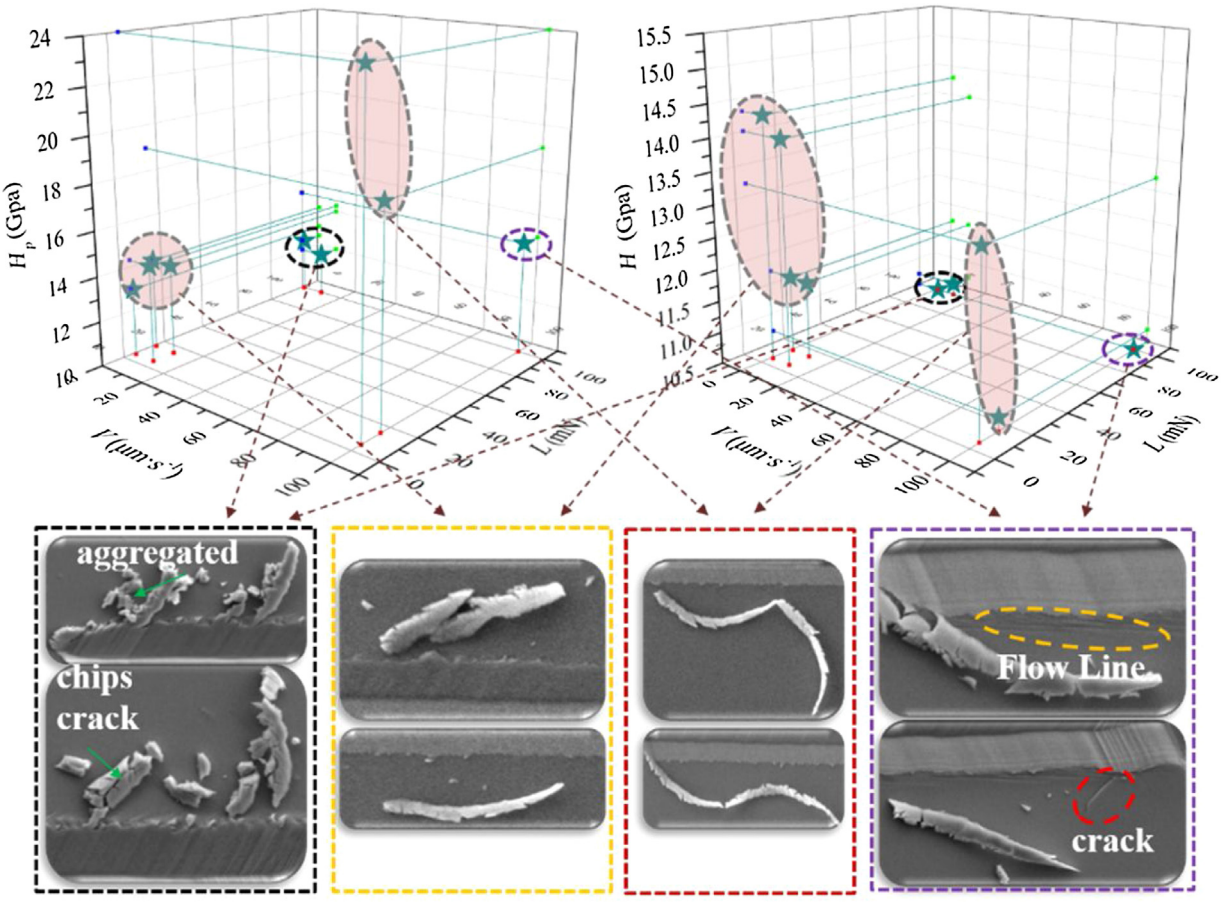

Fig. 10 – 3D plots of the relationships amount the two hardness distributions (H_p and H), scratching speed (V), and normal load (L), and the SEM micrographs of the surface morphologies corresponding to several representative points on the plots.

the scratch grooves, slight plastic flow lines at groove edge and uniform and complete debris. On the other hand, low degree of hardness dispersion is correlated with the relatively poor groove surfaces, where the flow lines are dense and cracks appear randomly on the groove edges.

4. Scratching and ploughing hardness distributions can be used as references for surface morphology evaluation as shown in the 3D plots. In addition, based on the intrinsic relationship between evolution of hardness and nanoscratch deformation modes, calculating hardness distribution by in-situ testing data and then adjusting deformation mode in real time can be advantageous when optimizing surface quality during surface preparation.

Conflict if interest

The authors declare no conflicts of interest.

Acknowledgments

This work was supported in part by the National Key Research and Development Program of China under Grant No. 2016YFB110225, and in part by Science Fund for Creative Research Groups of NSFC under Grant No. 51621064.

Appendix A.

Assume that the elastic deformation height of the material in front of the indenter caused by extrusion is equal to the elastic recovery depth of the material at the rear of the indenter, that is

$$h_e = h - h_f \tag{A1}$$

then according to the geometrical relationship in Fig. 4(c),

$$\Delta h = \frac{R}{\cos\left(\frac{1}{2}(\alpha+\beta)\right)}\cos\left(\frac{1}{2}(\beta-\alpha)\right) - R \tag{A2}$$

$$l_{CO} = \frac{R}{\cos\zeta} \tag{A3}$$

$$\gamma = \zeta - \alpha \tag{A4}$$

$$\zeta = \frac{\pi}{2} - (\alpha+\beta) \tag{A5}$$

$$S = S_{C1} + S_{C2} + S_{C3} \tag{A6}$$

$$S_{C1} = \sin\frac{\pi}{3}(h+\Delta h)^2\tan^2\left(\frac{\pi}{2}-\alpha\right) \tag{A7}$$

$$S_{c2} = 2\sin\frac{\pi}{3}\tan\left(\frac{\pi}{2}-\alpha\right)\tan\left(\frac{\pi}{2}-\beta\right)\cdot \tag{A8}$$

$$\left(h+\Delta h-h_f\right)(h+\Delta h)-\left(h+\Delta h-h_f\right)^2\tan^2\left(\frac{\pi}{2}-\beta\right)$$

$$S_{c3} = \sin\frac{\pi}{3}\tan^2\left(\frac{\pi}{2}-\alpha\right)\left(h+\Delta h-h_f\right)(h+\Delta h) \tag{A9}$$

The relationship between normal force and penetration depth is fitted by power function as:

$$h = \text{-}144L^{0.4} \tag{A10}$$

The relationship between the normal force and the average contact stress can be expressed as:

$$L = L_m S \tag{A11}$$

where L_m is average contact stress [39–42],

$$L_m = \lambda_0\left(m + k\ln\left(\frac{V}{w\dot{\varepsilon}}\right)\right)$$

$$\lambda_0 = \frac{2}{3}\frac{H_0}{2.8}\left(\frac{5}{3}+\ln\left(\frac{4(1-2\nu)\frac{H_0}{2.8}+E\tan\psi}{6(1-\nu)\frac{H_0}{2.8}}\right)\right)$$

Hence, h_f can be calculated as:

$$h_f = -2.8H_0 + \sqrt{-\frac{\left(\frac{h}{144}\right)^{2.5}}{4.3L_m}+\frac{79{H_0}^2}{4.3}} \tag{A12}$$

Appendix B.

$$COF = \frac{L_p}{L} \tag{B1}$$

$$L_p = \tau S_p \tag{B2}$$

$$L = L_m S \tag{B3}$$

$$L_m = \lambda_0\left(m + k\ln\left(\frac{V}{w\dot{\varepsilon}}\right)\right) \tag{B4}$$

REFERENCES

[1] Hostasa J, Necina V, Uhlirova T, Biasini V. Effect of rare earth ions doping on the thermal properties of YAG transparent ceramics. J Eur Ceram Soc 2019;39(1):53–8.

[2] Li C, Zhang F, Wu Y, Zhang X. Influence of strain rate effect on material removal and deformation mechanism based on ductile nanoscratch tests of Lu2O3 single crystal. Ceram Int 2018;44(17):21486–98.

[3] Mcmillen C, Thompson D, Tritt T, Lolis J. Hydrothermal single-crystal growth of Lu2O3 and lanthanide-doped Lu2O3. Cryst Growth Des 2011;11(10):4386–91.

[4] Iqbal F, Pyczak F, Neumeier S, Goken M. Crack nucleation and elastic / plastic deformation of TiAl alloys investigated by in-situ loaded atomic force microscopy. Mater Sci Eng: A 2017;689:11–6.

[5] Zhou SQ, Seita M. Large-area surface topography analysis of additively manufactured metallic materials using directional reflectance microscopy. Mater Sci Eng: A 2019;760:489–97.

[6] Khac BCT, DelRio FW, Chung KH. Interfacial strength and surface damage characteristics of atomically thin h BN, MoS2, and graphene. ACS Appl Mater Interfaces 2019;10(10):9164–77.

[7] Chen L, Wen JL, Zhang P. Nanomanufacturing of silicon surface with a single atomic layer precision via mechanochemical reactions. Nat Commun 2018;9(1):1542.

[8] Cai Y, Wang XS, Yuan SJ. Analysis of surface roughening behavior of 6063 aluminum alloy by tensile testing of a trapezoidal uniaxial specimen. Mater. Sci. Eng.: A 2016;672:184–93.

[9] He X, Cai C, Wang G, Zhao H, Xie L, Huang Y, Yan D, Ma P. Effect of pad elastic modulus on polishing induced subsurface damages distribution and laser-induced damage performance of fused silica optics. Opt Express 2019;27(1):265–81.

[10] Dikici T, Toparli M. Microstructure and mechanical properties of nanostructured and microstructured TiO2 films. Mater Sci Eng: A 2016;661:19–24.

[11] Catrin R, Neauport J, Legros P, Tarous D, Corbineau T, Cormont P, et al. Using STED and ELSM confocal microscopy for a better knowledge of fused silica polished glass interface. Opt Express 2013;21(24):29769–79.

[12] Ge M, Zhu H, Ge P, Zhang C. Investigation on residual scratch depth and material removal rate of scratching machining single crystal silicon with Berkovich indenter. Mater Sci Semicond Process 2019;100:98–105.

[13] Mosavat M, Rahimi A. Simulation and experimental study on the effect of abrasive size, rotational speed, and machining gap during ultra-precision polishing of monocrystalline silicon. Colloids Surf A Physicochem Eng Asp 2019;575:50–6.

[14] Chahboun A, Coratger R, Ajustron F, Beauvillain J, Aimar P, Sanchez V. Comparative study of micro- and ultrafiltration membranes using STM, AFM, and SEM techniques. Ultramicroscopy 1992;41(1-3):235–44.

[15] Klemenz A, Pastewka L, Balakrishna SG, Caron A, Bennewitz R, Moseler M. Atomic scale mechanisms of friction reduction and wear protection by graphene. Nano Lett 2014;14(12):7145–52.

[16] Chatterjee A, Polycarpoub A, Abelson J, Bellon P. Nanoscratch study of hard HfB2 thin films using experimental and finite element techniques. Wear 2010;268:677–85.

[17] Beake B, Vishnyakov V, Harris A. Relationship between mechanical properties of thin nitride-based films and their behaviour in nano-scratch tests. Tribol Int 2011;44(4):468–75.

[18] Chavoshi SZ, Gallo SC, Dong HS, Luo XC. High temperature nanoscratching of single crystal silicon under reduced oxygen condition. Mater Sci Eng: A 2017;684:385–93.

[19] Geetha D, Sophia PJ, Radhika R, RArivuoli D. Evaluation of nanoindentation and nanoscratch characteristics of GaN/InGaN epilayers. Mater Sci Eng: A 2017;683:64–9.

[20] Feng J, Wan Z, Wang W, Ding X, Tang Y. Crack behaviors of optical glass BK7 during scratch tests under different tool apex angles. Wear 2019;430:299–308.

[21] Huang L, Yao W, Mukherjee A, Schoenung J. Improved mechanical behavior and plastic deformation capability of ultrafine grain alumina ceramics. J Am Ceram Soc 2012;95(1):375–85.

[22] Wu Y, Huan H, Zou J. Lattice bending in monocrystalline GaAs induced by nanoscratching. Mater Lett 2012;80:187–90.

[23] Wasmer K, Parlinska-Wojtan M, Gassilloud R, Pouvreau C, Tharian J, Micher J. Plastic deformation modes of gallium arsenide in nanoindentation and nanoscratching. Appl Phys Lett 2007;90(3):0.1902.

[24] Mallikarjunachari G, Ghosh P. Pile-up response of polymer thin films to static and dynamic loading. Thin Solid Films 2019;677:1–12.
[25] Carreon A, Funkenbusch P. Material specific nanoscratch ploughing friction coefficient. Tribol Int 2018;126:363–75.
[26] Mallikarjunachari G, Ghosh P. Analysis of strength and response of polymer nano thin film interfaces applying nanoindentation and nanoscratch techniques. Polymer 2016;90:53–66.
[27] Chamani H, Ayatollahi M. Prediction of friction coefficients in nanoscratch testing of metals based on material flow lines. Theor Appl Fract Mech 2018;94:186–96.
[28] Saha R, Nix W. Soft films on hard substrates — nanoindentation of tungsten films on sapphire substrates. Mater Sci Eng: A 2001;319:898–901.
[29] Park S, Kim Y, Ruoff R, Kim J. Incipient plasticity and fully plastic contact behavior of copper coated with a graphene layer. APL Mater 2019;7(3):031106.
[30] Kucharski S, Woźniacka S. Size effect in single crystal copper examined with spherical indenters. Metall Mater Trans A 2019;50(5):2139–54.
[31] Zhang SH, Guo XG. Material removal characteristics of precorroded Lu2O3 laser crystals and elastic deformation model during nanoscratch process. Tribol Int 2020;143, http://dx.doi.org/10.1016/j.triboint.2019.106027 [online]. Availiable:.
[32] Wang Y, Raabe D, Klüber C, Roters F. Orientation dependence of nanoindentation pile-up patterns and of nanoindentation microtextures in copper single crystals. Acta Mater 2004;58(8):2229–38.
[33] Li C, Zhang F, Wang X, Rao X. Repeated nanoscratch and double nanoscratch tests of Lu2O3 transparent ceramics: material removal and deformation mechanism, and theoretical model of penetration depth. J Eur Ceram Soc 2018;38(2):708–18.
[34] Briscoe B, Sinha S. Scratch resistance and localised damage characteristics of polymer surfaces - a review. Materialwissenschaft and Werkstofftechnik 2010;34(10-11):989–1002.
[35] Williams J. Analytical models of scratch hardness. Tribol Int 1996;29(8):675–94.
[36] Li Z, Zhang F, Luo X. Fundamental understanding of the deformation mechanism and corresponding behavior of RB-SiC ceramics subjected to nano-scratch in ambient temperature. Appl Surf Sci 2019;469:674–83.
[37] Xu N, Han W, Wang Y, Li J, Shan Z. Nanoscratching of copper surface by CeO2. Acta Mater 2017;124:343–50.
[38] Mergler Y, Kampen R, Nauta W, Schaake R, Raas B, Griensver J, et al. Influence of yield strength and toughness on friction and wear of polycarbonate. Wear 2005;258(5-6):915–26.
[39] Li C, Li X, Wu Y, Zhang F, Huang H. Deformation mechanism and force modelling of the grinding of YAG single crystals. Int J Mach Tools Manuf 2019;143:23–37.
[40] Li C, Zhang F, Meng B, Rao X, Zhou Y. Research of material removal and deformation mechanism for single crystal GGG (Gd3Ga5O12) based on varied-depth nanoscratch testing. Mater Des 2017;125:180–8.
[41] Bhushan B. Principles and applications of tribology. New York: John Wiley & Sons; 2013.
[42] Zhang P, Li S, Zhang Z. General relationship between strength and hardness. Mater. Sci. Eng. A 2011;529:62–73.